Computer Modeling in Engineering & Sciences CMES, vol.123, no.1, pp.129-152, 2020

A Coupled Cavitation Model in an Oscillatory Oil Squeeze Film

Xu Liu[1], Xiaoyang Chen[1, *], Rongyu Kang[1], Xuejin Shen[1] and Ben Ni[2]

Abstract: In this paper, the oscillatory oil squeeze film is taken as a research object, and a coupled cavitation model based on the theory of bubble dynamics and hydrodynamic lubrication is used and a specific method of numerical calculation is given. Then the parallel-plate squeeze film test apparatus is used to validate the coupled cavitation model. The pictures of the cavitation were captured by a high-speed camera and then processed to obtain the variation of the cavitation area in experiments. Compared with the experimental results, the model can successfully predict the process of generation and development of cavitation. At the same time, the pressure variation calculated by the model is in good agreement with the experimental data and the value of negative pressure is close to the experiment. On this basis, three new parameters that are related to bubble dynamics are studied by comparing the pressure and cavitation area variation in an oscillating squeeze oil film. The results show that surface dilatational viscosity, initial radii of cavitation nuclei and number of bubbles per unit area have a significant influence on the generation time of the cavitation, the maximum tensile stress that the oil film can withstand, and the speed of the cavitation collapse respectively.

Keywords: Bubble dynamics, oscillatory oil squeeze film, cavitation.

1 Introduction

In lubricated mechanical systems, oil is widely used as a thin film to reduce wear and to create damping to eliminate undesirable mechanical vibrations. The phenomenon that oil film may fracture in tensile stress is called cavitation. According to the formation mechanism, cavitation is divided into three forms [Braun and Hannon (2010); Geike and Popov (2009)]:

(1) Gaseous cavitation, where cavitation arises from dissolved gases in fluid when the pressure falls below the saturation pressure.

(2) Pseudo-cavitation, which expands due to depressurization without further gas mass diffusion.

(3) Vapor cavitation, which develops when the pressure falls below the saturation pressure.

Experiments show that the developments and collapse of cavitation are common in bearing systems. It is well known that the divergent region of hydrodynamic bearing will generate cavitation under static load. However, when bearings work under a dynamic load, the

[1] Shanghai University, Shanghai, 200072, China.

[2] Ford Motor Company, Dearborn, MI 48126, USA.

[*] Corresponding Author: Xiaoyang Chen. Email: xychen@shu.edu.cn.

Received: 03 July 2019; Accepted: 16 January 2020.

dynamic cavitation phenomenon becomes complex. In order to study the dynamic changes of cavitation, the high-speed camera was used to take pictures of cavitation. Natsumeda and Someya found two different shapes of initial cavitation: one is fern cavitation; the other is small circular cavitation by using a high-speed camera [Natsumeda and Someya (1987)]. Sun et al. obtained better cavitation photographs through their experimental equipment and concluded that: the cavitation first appeared in the center of the oil film low-pressure zone, then became larger and finally disappeared [Sun and Brewe (1991)]. However, the pressure of the oil film could not be collected during the experiment. To figure out the composition of the cavitation, Sun and Brewe improved the experimental equipment so that visualization and pressure acquisition could be conducted simultaneously [Sun, Brewe and Abel (1994)]. Through experiments, it is concluded that the cavitation contains oil vapor, which may also contain air, and the negative pressure of the cavitation is close to the absolute zero pressure. Dellis conducted a series of experiments [Dellis (2019, 2005); Dellis and Arcoumanis (2005)] and found the changing process of cavitation developments in oil film and three shapes cavities which are fern cavities, fissure cavities, and string cavities. So high-speed camera is an effective way to study the dynamic changes of cavitation.

To better understand the time-dependent cavitation under a dynamic load, many researchers conducted experiments in squeeze film to eliminate the influence of wedge effect. Hays et al. put phosphor into oil between two parallel plates to make it easier to take cavitation pictures [Hays and Feiten (1964)]. However, the existence of phosphor in oil will affect the development of cavitation, which is quite different from the real situation. Parkins et al. recorded pressure values and took corresponding oil film photos in their parallel plate experiments, but those photos were not clear [Parkins and May-Miller (1984)]. Sun et al. compared the characteristic times of the two kinds of cavitation [Sun and Brewe (1992)]. They concluded that gaseous cavitation in SFDs should only be related to air ingestion. Chen used the squeeze oil film test apparatus to study cavitation change with time and found that under certain working conditions, tensile stress and cavity existed simultaneously [Chen, Sun, Wang et al. (2004)]. The oil film can withstand a certain negative pressure, and the cavitation is uniformly diffused in each direction, so the cavitation is generated from the middle of the plate. The high-speed camera was used to capture the cavitation dynamic change and the fern-shaped cavitation was found. However, the reason for the formation of cavitation of different shapes has not been systematically analyzed. Wang used electromagnetic vibrator squeeze oil film experiments to carry out pressure collection and compared the pressure with calculated results [Wang, Zhang, Chen et al. (2005)]. However, the displacement curve driven by the electromagnetic exciter changes greatly, and the experiment does not achieve good results. Sun proposed a cavitation model which combined with the basic bubble dynamics in the oscillatory oil squeeze film [Sun, Wang, Zhang et al. (2008)]. Sun conducted an experimental study about cavitation in oscillatory oil squeeze film to verify his model [Sun, Zhang, Chen et al. (2008)]. It is found that the testing pressure curve is consistent with the cavitation model; at the same time, the influence of nuclei on cavitation is also considered. However, the cavitation area variable in the experiment is much larger than the theoretical calculation. Zarbane studied cavitation in squeeze film dampers with digital camera [Zarbane, Zeghloul and Hajjam (2013, 2011)]. They found two film

rupture modes which were mainly determined by oscillations frequency and gaseous cavitation was related to air ingestion.

Based on the experiments, various cavitation algorithms were proposed one after another. Jakobsson, Floberg et al. proposed a cavitation model that considered the equilibrium of lubricant flow at the oil film rupture and re-formation boundary. This boundary model is called the mass conservation boundary model [Floberg (1961); Olsson (1965); Jakobsson and Floberg (1957)], also known as the JFO boundary model. The JFO boundary condition not only provides the rupture condition of the oil film but also considers the process of regeneration of the oil film. However, the initial JFO boundary conditions require dynamic tracking, which is cumbersome to use. Based on the assumption of lubricant incompressibility, Elord proposed the famous Elrod algorithm [Elrod (1981)]. By introducing a new variable θ and a switching function g, the full oil film region and cavitation region are unified into a general equation, and the dynamic boundary is automatically determined in the numerical calculation process. Later, some researchers further improved Elrod algorithm, including Brewe [Brewe (1986)], Vijayarahavan et al. [Vijayaraghavan and Keith Jr (1989)], Kumar et al. [Kumar and Booker (1991)], Vincent et al. [Vincent, Maspeyrot and Frene (1996)], Bayada et al. [Bayada, Chambat and Alaoui (1990)] and Olson et al. [Olson and Booker (1997)]. They all proposed different cavitation algorithms based on the mass conservation boundary model. However, it is known that the cavitation is linked with the existence and evolution of cavitation nuclei in liquid which has been neglected in their models until Someya's work was published [Natsumeda and Someya (1987)]. The RP equation was used to model the presence of air bubbles in the lubricant of a journal bearing. Diaz was the first to introduce RP equation in SFDs to deal with the gaseous cavitation in SFDs [Diaz Briceno (1999); Diaz and San Andres (2001)]. They used a simplified form RP equation and the reference volume fraction of the air ingestion in through the outlet portion was estimated by the mass balance equation. They found that high void fraction decreased the capability of the fluid to sustain tension by experiments. In recent years, the notion that combines achievements in bubble dynamics and hydrodynamic lubrication has gained much attention and gotten continuous improvement in works of Gehannin et al. [Gehannin, Arghir and Bonneau (2016)], Geike et al. [Geike and Popov (2009, 2009)] and Snyder et al. [Snyder and Braun (2019); Snyder, Braun and Pierson (2016, 2015)]. In 2017, Braun made a preliminary review of this filed and proposed a two-way coupling algorithm [Braun, Pierson and Snyder (2017)]. Recently a stable algorithm that couples Reynolds and Rayleigh-plesset equation has been proposed by Jaramillo et al. [Jaramillo and Buscaglia (2019)]. This method can guarantee absolute convergence in the process of computational iteration. However, most of their research objects are static load bearing. Besides, this concept lacks relevant experimental verification, especially in comparison with the process of cavitation dynamics. Therefore, the main work of this paper is taking an oscillatory oil squeeze film as the research object and carrying out related cavitation model. In order to study the difference between this cavitation model and the actual cavitation in an oscillatory oil squeeze film, a high-speed camera is used to take pictures of variation of cavitation in oscillatory parallel plate squeeze oil film. The calculated pressure variation curve and the testing pressure variation curve in Sun's experiments

[Sun, Zhang, Chen et al. (2008)] are compared. Finally, the effects of parameters on oil film pressure and cavitation area are studied.

2 Modeling

2.1 Bubble dynamics

The Rayleigh equation describes the transient pressure distribution of the liquid around a single bubble and the change of the bubble diameter with time:

$$R\bullet\ddot{R}+\frac{3}{2}\dot{R}=\frac{p_R-p_\infty}{\rho} \tag{1}$$

where R is bubble radius, p_R is the pressure at bubble's exterior surface, p_∞ is the pressure of the fluid at far field, ρ is liquid density. This equation lays the foundation for classical bubble dynamics. For oscillatory motion, the lubricating oil will develop the interfacial viscous properties κ_s, called surface dilatational viscosity [Gehannin, Arghir and Bonneau (2009)]. The surface dilatational viscosity stress is an excessive stress, which acts to provide a dissipation resistance for temporarily restoring equilibrium. So, it has a damping effect on bubble growth and collapse. And Snyder suggested that the viscous effects within the bubble could be neglected [Snyder, Braun and Pierson (2016)]. If the liquid is considered as Newtonian incompressible liquid, the pressure at bubble's exterior surface will be:

$$p_R=p_B-\frac{4\mu_L}{R}\frac{dR}{dt}-\frac{2\sigma}{R}-\frac{4\kappa^s}{R^2}\frac{d^2R}{dt^2} \tag{2}$$

where p_B is the inside pressure of the bubble, μ_L is the viscosity of liquid, σ is surface tension. Then replacing p_R in Eq. (1) by using its expression in Eq. (2) can lead to a bubble dynamics equation:

$$R\bullet\ddot{R}+\frac{3}{2}\dot{R}^2=-\frac{4\nu_{\mathrm{L}}\dot{R}}{R}-\frac{4\kappa^s\dot{R}}{\rho_L R^2}-\frac{2\sigma}{\rho_L R}+\frac{p_B-p_\infty}{\rho_L} \tag{3}$$

If the bubble does not contain oil vapor, the Eq. (3) will become:

$$\rho_L(R\bullet\ddot{R}+\frac{3}{2}\dot{R}^2)=-(\mu_{\mathrm{L}}+\frac{\kappa_s}{R})\frac{4}{R}\dot{R}+P_0(\frac{R_0}{R})^{3k}-\frac{2\sigma}{R}-p \tag{4}$$

where P_0 is the inner pressure when the bubble radius is equal to R_0 and R_0 is initial radii of cavitation nuclei. Then we can define:

$$F(R)=P_0(\frac{R_0}{R})^{3k}-\frac{2\sigma}{R} \tag{5}$$

$$G(R)=\frac{R}{4\mu_{\mathrm{L}}+\frac{4\kappa_s}{R}} \tag{6}$$

Many researchers suggest that the inertial terms in Eq. (4) can be neglected, so combining with Eqs. (5) and (6), Eq. (4) becomes:

$$\frac{dR}{dt}=G(R)(F(R)-p) \tag{7}$$

If there is a larger number of bubbles in a field and these bubbles are assumed to be evenly distributed, considering the velocity field of the bubbles $\vec{V} = (u, v, w)$ and $\vec{R}(x,t)$, one can get:

$$\frac{\partial R}{\partial t} + \vec{V} \cdot \nabla R = G(R)(F(R) - p) \tag{8}$$

In Eq. (8), there are two unknown variables (R and p). So, we need additional equations to close this system.

2.2 Governing equations in an oscillatory oil squeeze film

The research object of this paper is an oscillatory oil squeeze film. We assume that this oscillatory oil squeeze film is between two parallel circular plates. The lower plate is fixed, and the upper plate moves up and down along the normal direction, as shown in Fig. 1. The gap between the two plates' surface h is filled with Newtonian lubricant. The density ρ and viscosity μ of the lubricant are given.

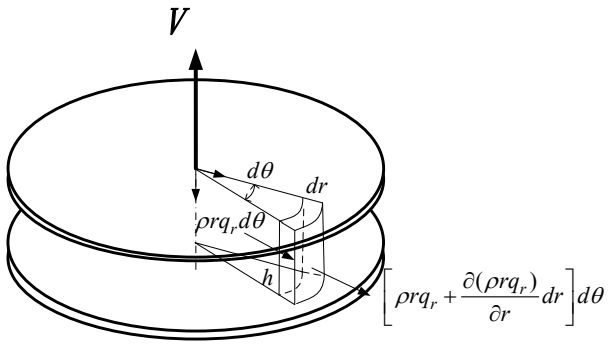

Figure 1: Schematic of an oscillatory oil squeeze film

As shown in Fig. 1, a circular cylindrical coordinate is established for the oil film, where *r, θ, y* represents the radial coordinate, circumferential and axial (film thickness direction) coordinates respectively. Taking the columnar control space, the net outflow during time *dt* is:

$$\frac{\partial(\rho r q_r)}{\partial r} dr d\theta dt \tag{9}$$

Notice that for the oscillatory oil squeeze film, there is no circumferential motion between the two parallel plates. As a result, there is no circumferential flow in fluid. Therefore, the liquid outflow and inflow of the two surfaces in the circumferential direction of the control body are not considered in this paper.

At the same time, the instantaneous speed of the upper plate V causes the volume expansion of the control space. So, the amount of change in the mass in the space is:

$$\frac{\partial(\rho h)}{\partial t} dr \cdot r d\theta dt \tag{10}$$

Due to the conservation of fluid mass in the controlled volume, it is available that:

$$\frac{\partial(\rho r q_r)}{\partial r} - r\frac{\partial(\rho h)}{\partial t} = 0 \tag{11}$$

where q_r is radial flow in the controlled volume. It's known that

$$q_r = -\frac{h^3}{12u}\frac{\partial p}{\partial r} \tag{12}$$

Combining Eqs. (11) and (12), one can get

$$\frac{\partial}{\partial r}\left(\frac{r\rho h3}{12\mu}\frac{\partial p}{\partial r}\right) = \rho r\frac{\partial h}{\partial t} + r\frac{\partial \rho}{\partial t}, \tag{13}$$

along with the boundary condition

$$p\big|_{r=a} = p_{atm} \tag{14}$$

To couple bubble and governing equations for hydrodynamic lubrication, we make an assumption that there are a large number of cavitation nuclei suspending in oil film between two parallel plates, as shown in Fig. 2, and they are considered as gas nuclei. It should be noted that in the oil film, the radii of the cavitation nuclei are very small and are invisible to naked eyes. The size of cavitation nuclei is enlarged to illustrate in Fig. 2.

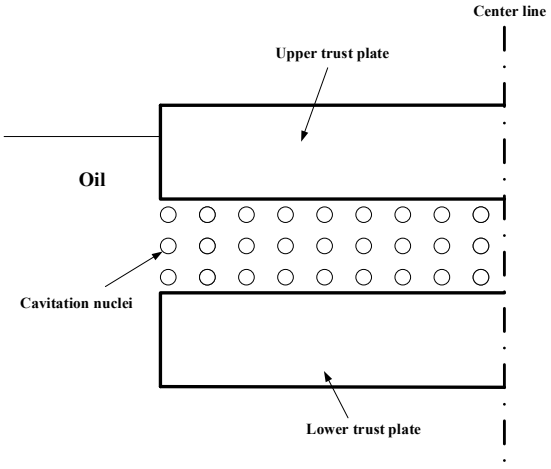

Figure 2: Cavitation nuclei suspending in oil film

To simplify this problem, we assume that the cavitation nuclei are uniformly dispersed in the lubricating oil and do not affect each other. During the downward movement of the upper plate, the oil film between the two parallel plates is under compression stress, as is shown in Fig. 3.

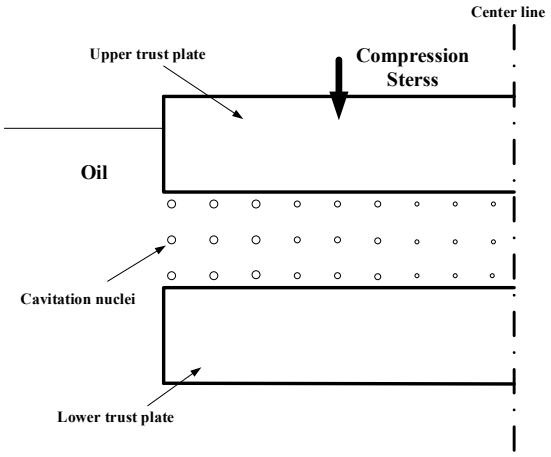

Figure 3: Cavitation nuclei under compression stress

According to bubble dynamics, the gas nuclei become smaller under compression stress. In this situation, the cavitation nuclei can be neglected so that the lubricants between two plates can be regarded as full oil film region. On the contrary, during the upward movement of the upper plate, the oil film between the two parallel plates is under tension stress, as is shown in Fig. 4.

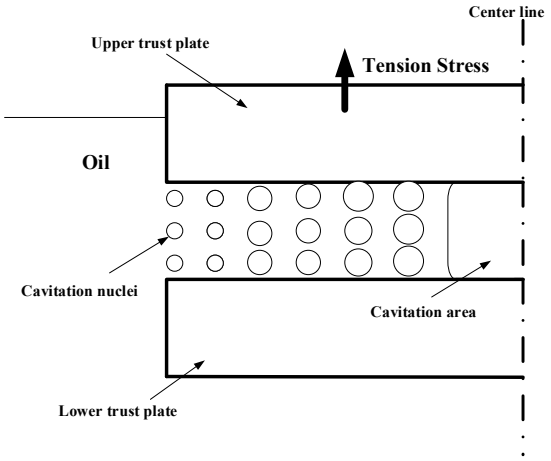

Figure 4: Cavitation nuclei under compression stress

Under the tension stress, cavitation nuclei develop into visible bubbles. Then the oil film could become mixture of lubricants and cavitation. When the tensile stress is high enough, these bubbles will empty the lubricant between two plates and become cavitation region.

It can be noted that the bubble being spherical in lubricants under large disturbances is idealized since the local wall effect and bubble interaction may destroy the shape of spherical bubble. However, the specific shape of the bubble is not considered to limit the effectiveness of the bubble dynamics equation. Meanwhile, there is no simple or practical alternative method for non-spherical bubble dynamics, so it is acceptable to assume that the bubble is always spherical.

On this basis, we define the fraction variable:

$$\alpha=\frac{\text{volume of gas}}{\text{volume of gas and liquid}} \tag{15}$$

After knowing this variable, the density $\rho(\alpha)$ and viscosity $\mu(\alpha)$ of mixture can be obtained. According to its expression, the fraction variable depends on the number and size of bubbles. The number concentration of bubbles n_b could be a given parameter according to Alfredo [Jaramillo and Buscaglia (2019)]. And if we assume that the bubbles are spherical in liquid, we can get the algebraic relation of fraction variable [Singhal, Athavale, Li et al. (2002); Zwart, Gerber and Belamri (2004)]:

$$\alpha=\frac{V_{\text{bubbles}}}{V_{cell}}=n_b\frac{4}{3}\pi R^3 \tag{16}$$

Given that the number concentration of bubbles n_b is a given parameter, the fraction variable α is only related to bubble radius *R*. Due to the uniformity of cavitation nuclei distribution, the number of bubbles per unit volume can be computed as $n_b=n_b^{\mathrm{s}}/h$, where n_b^{s} is the number of bubbles per unit area. So, Eq. (16) become

$$\alpha=\left(\frac{n_b^{\mathrm{s}}}{h}\right)\frac{4}{3}\pi R^3 \tag{17}$$

After obtaining the fraction variable α, the mixture density and viscosity can be gained

$$\rho(\alpha)=(1-\alpha)\rho_l+\alpha\rho_g \tag{18}$$

$$\mu(\alpha)=(1-\alpha)\mu_l+\alpha\mu_g \tag{19}$$

Thus, through Eqs. (18) and (19), we can get the viscosity and density of the mixture when the volume fraction at this moment is gained through the calculation from the cavitation bubble radius. Then putting the new viscosity and density into Eq. (13), one can get the pressure distribution in the oscillatory oil squeeze film. In turns, having known the pressure distribution in oil film, one can obtain the bubble radius by using the expression in Eq. (8) in this condition. Through this method, the bubble dynamics and hydrodynamic lubrication are effectively coupled together. The specific solution and steps will be introduced in the next section.

2.3 Numerical method

Considering the symmetry of the circular plate, finite volume scheme was used with sector cells of length Δx along the radial direction. Meanwhile, a constant time step Δt was used.

If Eq. (8) is integrated explicitly by first order, the bubble radii at the next time level (n+1) will meet the following equation:

$$R_i^{\mathrm{n+1}}=R_i^{\mathrm{n}}+\Delta t\left\{G(R_i^{\mathrm{n+1}})\left[F(R_i^{\mathrm{n+1}})-p_i^{\mathrm{n}}\right]-\overline{u}\frac{dR_i^{\mathrm{n}}}{dx}\right\} \tag{20}$$

where $\overline{u}$ is average film velocity in the radial direction and it is computed as

$$\overline{u}=-\frac{h_i^2}{24\mu_i^n\Delta x}(p_{i+1}^n-p_{i-1}^n) \tag{21}$$

And $\frac{dR_i^{\mathrm{n}}}{dx}$ is discretized by mean of the upwind scheme as

$$\frac{dR_i^{\mathrm{n}}}{dx}=\frac{R_i^{\mathrm{n}}-R_{i-1}^{\mathrm{n}}}{\Delta x} \text{ if } \overline{u}>0 \tag{22}$$

$$\frac{dR_i^{\mathrm{n}}}{dx}=\frac{R_{i+1}^{\mathrm{n}}-R_i^{\mathrm{n}}}{\Delta x} \text{ if } \overline{u}<0 \tag{23}$$

If the bubble radii for all cells have already been calculated, the fraction variable can be obtained by using Eq. (17). However, bubbles may develop until they touch one another or fill all the volume between two plates, as is discussed above. To deal with this full cavitation region problem, it is necessary to give fraction variable an upper limitation as

$$\alpha=\min\left(\left(\frac{n_b^{\mathrm{s}}}{h}\right)\frac{4}{3}\pi R^3,1\right) \tag{24}$$

Meanwhile, when fraction variable is equal to 1, the following value was given to bubble radius:

$$\begin{aligned}&\frac{dR}{dt}=G(R)(F(R)-p) \text{ if } \alpha<1\\&R=\sqrt[3]{\left(\frac{3h}{4\pi n_b^s}\right)} \qquad \text{if } \alpha\geq 1\end{aligned} \tag{25}$$

Eq. (13) can be discretized as

$$\frac{1}{\Delta x^2}(M_{i-\frac{1}{2}}p_{i-1}^{n+1}-(M_{i-\frac{1}{2}}+M_{i+\frac{1}{2}})p_i^{n+1}+M_{i+\frac{1}{2}}p_{i+1}^{n+1})=\frac{r_i}{\Delta t}((\rho h)_i^{n+1}-(\rho h)_i^n) \tag{26}$$

with

$$M_{i\pm\frac{1}{2}}=\frac{r_i\rho_i^{n+1}(h_i^n)^3/(12\mu)+r_{i+1}\rho_{i\pm1}^{n+1}(h_{i\pm1}^n)^3/(12\mu)}{2} \tag{27}$$

The above equation may be rearranged to read:

$$A_i p_{i-1}^{n+1}+B_i p_i^{n+1}+C_i p_{i+1}^{n+1})=D_i \tag{28}$$

where

$$A_i=\frac{1}{\Delta x^2}M_{i-\frac{1}{2}} \tag{29}$$

$$B_i=-\frac{1}{\Delta x^2}(M_{i-\frac{1}{2}}+M_{i+\frac{1}{2}}) \tag{30}$$

$$C=\frac{1}{\Delta x^2}M_{i+\frac{1}{2}} \tag{31}$$

$$D_i=\frac{r_i}{\Delta t}\left(\left(\rho h\right)_i^{n+1}-\left(\rho h\right)_i^{n}\right) \tag{32}$$

After solving Eq. (28), one can get the new pressure distribution p^{n+1}. Repeat using Eqs. (20)-(23), bubble radius for next time iteration R_i^{n+2} could be obtained. Then the pressure for next time iteration p^{n+2} can be obtained by using Eqs. (18)-(19) and Eqs. (25)-(32) By continuously repeating the process, the pressure variation over the whole-time cycle can be obtained.

3 Numerical simulation and experiment

In the above process, the influence of the local wall and the interaction between the bubbles are neglected and so is the effect of the inertial force in the process of using the bubble dynamics equation. In order to study whether the neglect of these parameters will have a large impact on the theoretical results, it is necessary to verify the numerical simulation by experiments. So, a parallel-plate squeeze film test apparatus was built to study the variation of cavitation in real oscillatory oil squeeze film. The schematic and photograph of this test apparatus are shown in Fig. 5 and Fig. 6.

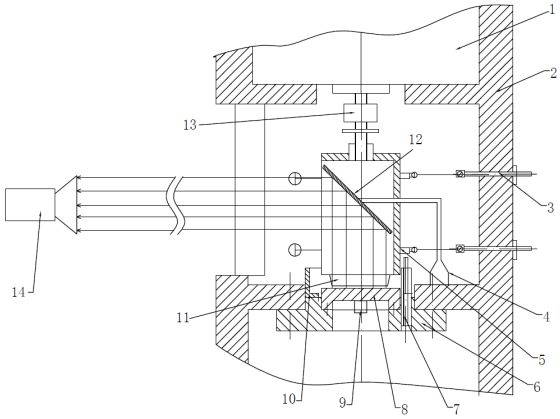

1-electromagnetic exciter 2-stationary housing 3-pull-rods and spring wires
4-mirror with support 5-movable frame 6-base plate 7-displacement sensor
8-lower thrust plate 9-vibration sensor 10-wall of oil pool
11-upper transparent plate 12-mirror 13-force sensor 14-high-speed camera

Figure 5: Schematic of parallel-plate squeeze film test apparatus

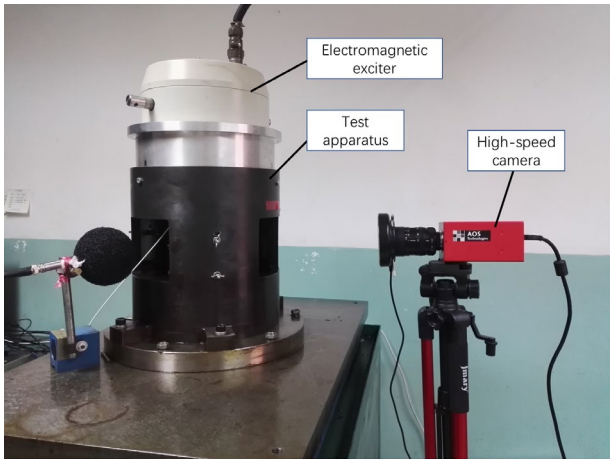

Figure 6: Photograph of test apparatus

The core components of this test apparatus include a lower plate (8) and an upper plate (11). The upper one is transparent and made of optical K9 glass. It is 25 mm thick and 50 mm in diameter and is fixed to the movable frame (5). The lower thrust plate is 60 mm in diameter and is fixed to the base plate (6). Three displacement sensors (7) are installed on the base plate to test the gap between two plates and help adjust the parallelism between the two plates. The base plate is fixed to the stationary housing (2). An adjustable coupling between the electromagnetic exciter (1) and the movable frame is used to adjust the initial oil film thickness between two plates. The parallelism between the lower and upper plates is set by adjusting six spring wires (3). These steel wires are divided into upper and lower groups, and each group has three wires distributed at 120 degrees. One end of each wire is attached to the movable frame and the other end is attached to the stationary housing. So, the taut steel wires assure the true vertical motion between two plates. Two plates are submerged in oil confined by the wall of the oil pool (10). A 45° mirror (4) is placed above the upper plate and fixed on stationary housing. Through the reflection of the mirror, the change of the cavitation in the oscillatory oil squeeze film can be observed in the horizontal direction. The high-speed camera can output up to 2500 frames per second with 320×320 pixels and keep writing image data to the PCI-E solid-state drive (SSD) until it is full. Given that the microjet is not the object of study, 500 fps is clear enough to observe the dynamic change of the cavitation area. A LED lighting is used to illuminate the test apparatus. When the upper plate moves in a vertical direction by using an electromagnetic exciter, the change of cavitation is observed through the transparent plate and mirror with a high-speed camera. At the same time, the displacement is measured with displacement sensors. The experimental condition is shown in Tab. 1. The oscillatory squeeze was set as 10 Hz and sampling frequency was 48000 Hz for displacement sensors. The oil used was ISP-VG #32, whose density was 872 kg/m^3 and viscosity was 32 mm^2/s at 40°C and 5.6 mm^2/s at 100°C. The input signal was a sine wave and the signal was amplified by a power amplifier.

Table 1: Experiment conditions

Experiment conditions	Parameter	Experiment conditions	Parameter
Plate diameter	50 mm	Lubricating oil type	ISO-VG 32
Lower plate material	S45C steel	Sampling frequency	48000 Hz
Upper plate material	K9 glass	The input signal	Sine wave
Squeeze frequency	10 Hz	Acquisition rate of high-speed camera	500 fps

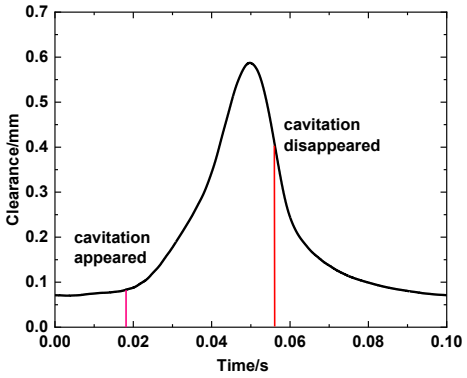

Figure 7: Displacement variation in one cycle

A random experimental cycle is selected for analysis. The clearance between the two plates was shown in Fig. 7, which was measured by one displacement sensor. From this curve, it can be found that the measured displacement curve is not a strict sine curve. It is the result of the changing oil film force and the inner spring of the exciter. At the same time, the photos of cavitation in oil film are shown in Fig. 8.

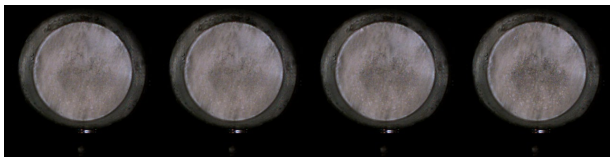

0.018 s 0.020 s 0.022 s 0.024 s

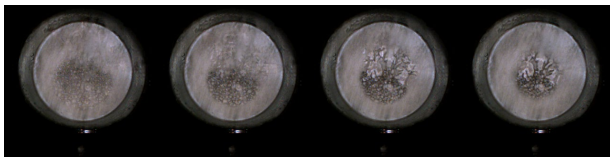

0.026 s 0.028 s 0.030 s 0.032 s

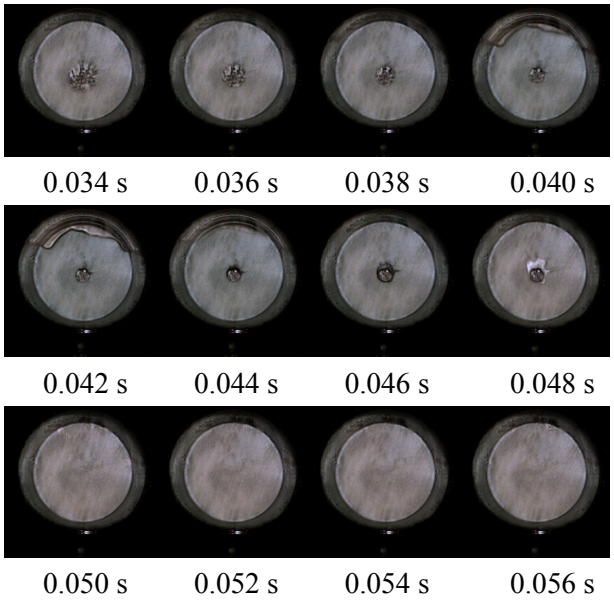

Figure 8: Cavitation photos in one cycle

These are pictures of a complete cycle taken by a high-speed camera. The pictures before 0.018 s and after 0.056 s are not listed because of no cavitation in them. It can be observed that cavitation starts from 0.020 s, then gradually develops and reaches a maximum at 0.030 s. After that, the cavitation gradually decreases and finally disappears after 0.050 s. By picture processing, the diameter of the envelope of cavitation area can be measured. So, the variation of cavitation area during one cycle is plotted in Fig. 9.

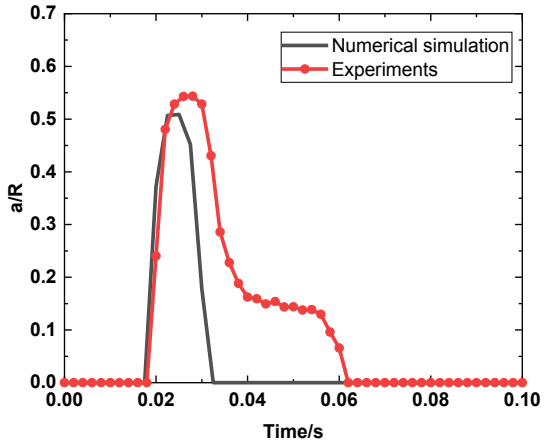

Figure 9: Measured size variation of cavitation in one cycle

In simulations, domain corresponds to a cylindrical shape, of which lower base diameter is L=50 mm (plate diameter) and the height is the clearance of two plates h. In fact, considering the symmetry of the cylinder, it is only necessary to solve the pressure and bubble radius in the diameter direction [-25 mm, 25 mm]. The grid length along diameter

direction was set to $\Delta x = L/1025$. For comparison, the change of oil film clearance is taken from the data actually collected by the displacement sensor in experiments, as shown in Fig. 7. As a result, the time step was set to $\Delta t = 1/f$, where f is the sampling frequency and f=48000Hz. The values of the other parameters are shown in Tab. 2. Viscosity μ and density ρ of lubricating oil refer to ISO-VG #32 lubricating oil at ambient temperature. The values of the number of bubbles per unit area n_b^s, surface dilatational viscosity κ^s and initial radii of cavitation nuclei R_0 are recommended values in the reference [Snyder, Braun and Pierson (2016)]. Eq. (20) was integrated by using a MATLAB function "ode23" from initial radii of cavitation nuclei R_0 at $t = 0s$. After R was obtained for a time step, α was evaluated according to Eq. (24). The discretization process of Eq. (28) produces a sparse matrix made up primarily by tri-diagonal elements the form as shown in Eq. (33).

$$\begin{bmatrix} 1 & & & & & & & & & \\ A_1 & B_1 & C_1 & & & & & & & \\ & \ddots & \ddots & & & & & & & \\ & & \ddots & \ddots & & & & & & \\ & & & A_i & B_i & C_i & & & & \\ & & & & \ddots & \ddots & \ddots & & & \\ & & & & & \ddots & \ddots & \ddots & & \\ & & & & & & A_{n-1} & B_{n-1} & C_{n-1} & \\ & & & & & & & & 1 & \end{bmatrix} \begin{bmatrix} p_1 \\ p_2 \\ \vdots \\ \vdots \\ p_i \\ \vdots \\ \vdots \\ p_{n-1} \\ p_n \end{bmatrix} = \begin{bmatrix} p_{atm} \\ D_2 \\ \vdots \\ \vdots \\ D_i \\ \vdots \\ \vdots \\ D_{n-1} \\ p_{atm} \end{bmatrix} \tag{33}$$

The Tri-Diagonal Matrix Algorithm (TDMA) was used in the process of solving this sparse matrix. The results calculated by the numerical simulation are also drawn in Fig. 9 and the variation of fraction variable and bubble radius are shown in Fig. 10.

Table 2: Parameters values

Parameters	Values	Parameters	Values
Oil Viscosity μ_L	0.0304 Pa·s	Oil Density ρ_L	872 kg/m^3
Air Viscosity μ_G	1.81×10^{-5} Pa·s	Air Density ρ_G	1 kg/m^3
Surface tension σ	0.0304 N/m	Number of bubbles per unit area n_b^s	1.91×10^{11} m^{-2}
surface dilatational viscosity κ^s	7.85×10^{-6} N·s/m	Initial radii of cavitation nuclei R_0	0.385×10^{-6} m
Atmospheric pressure	100 kPa		

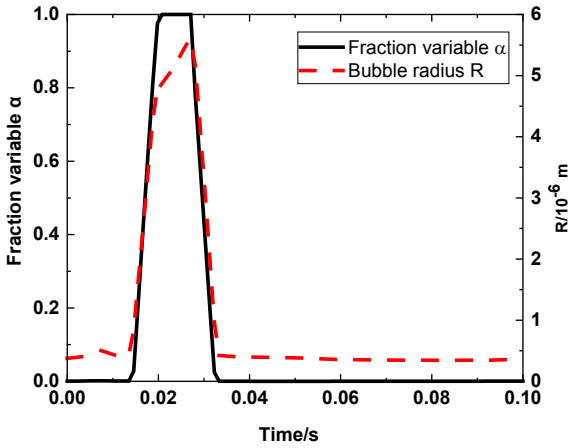

Figure 10: Calculated variation of fraction variable and bubble radius in one cycle

When the fraction variable α >0.98, this position is considered to be cavitation region, as shown in Fig. 10. It should be noted that in full cavitation region, due to the increase of clearance h, bubble radius R will increase slightly according to Eq. (25). In Fig. 9, the cavitation area variation calculated by the coupled model is well fitted to the experimental curve, especially at the beginning and the growth phase of the cavitation. Moreover, the error of the maximum cavitation area between numerical simulation and experiment is within 10%. In the collapse process of the cavitation, the calculated curve declines steeply, but the experimental curve yields a slower drop, indicating that the cavitation collapse velocity obtained by numerical simulation is slightly larger than that obtained by experiments. Meanwhile, there is an interesting phenomenon in the experiment that the collapse process of the cavitation seems to be blocked at about 0.04 s. This may be the cohesion of the cavity itself or the influence of the upper and lower walls. It is suspected that the phenomenon is the result of the cavitation inertial force or the effect of the upper and lower walls, which suggests that further work needs to be done to improve the model in cavitation collapse stage in the future. Still, this is a big step forward from previous models.

In summary, the experiment conducted by the parallel-plate squeeze film test apparatus shows that for the oscillating squeeze oil film, the model can successfully predict the generation and development of cavitation and the maximum envelope area of cavitation, which proves the reliability of the model. However, the test machine was unable to be installed with a pressure sensor due to insufficient internal space, so the pressure between the parallel plates cannot be collected. In order to further verify the accuracy of the model, this paper uses Sun's experimental pressure data [Sun, Zhang, Chen et al. (2008)] to verify the results of the pressure calculated by the model. In Sun's experiments, the experiment conditions are listed as follows:

The oil used was ISO-VG #68 and the plate diameter was 50 mm. The squeeze frequency was 5 Hz. The oscillatory squeezing motion was driven by the eccentric cam, so the displacement curve was a sinusoid curve which satisfied the equation

$$h = h_0 - \varepsilon \sin(\omega t) \tag{34}$$

where the equilibrium position h_0 is 234 μm, the amplitude ε is 139 μm and the frequency ω is 5 Hz. During calculation, the values of the other parameters' values are as shown in Tab. 3. The grid length along diameter direction was set to $\Delta x = L/1025$ as before, while the time step was set to $\Delta t = 5\times10^{-6}$ s. The change of oil film clearance at each time step was calculated by Eq. (34).

Table 3: Parameters values

Parameters	Values	Parameters	Values
Oil Viscosity μ_L	0.070 Pa·s	Oil Density ρ_L	865 kg/m^3
Air Viscosity μ_G	1.81×10^{-5} Pa·s	Air Density ρ_G	1 kg/m^3
Surface tension σ	0.035 N/m	Number of bubbles per unit area n_b^s	1.91×10^{11} m^{-2}
surface dilatational viscosity κ^s	7.85×10^{-6} N·s/m	Initial radii of cavitation nuclei R_0	0.385×10^{-6} m
Atmospheric pressure	100 kPa	Residual rate β (for Sun's model)	1/3
Internal pressure in the cavitation region p_v (for Sun's model)	30 Pa		

Meanwhile, Sun also proposed his own cavitation model. According to his model, the pressure in the oscillatory oil squeeze film is that

$$p=3\mu r^2\frac{h'}{h^3}-3\mu\frac{h'}{h^3}\frac{1}{\ln\frac{a}{\bar{R}}}\left[a^2\ln\frac{r}{\bar{R}}+R^2\ln\frac{r}{\bar{R}}\right]+\frac{1}{\ln\frac{a}{\bar{R}}}\times\left\{p_a\ln\frac{r}{\bar{R}}+[p_v-\sigma(\frac{1}{\bar{R}}+\frac{2\cos\bar{\alpha}}{h})]\ln\frac{a}{r}\right\} \tag{35}$$

where

$$\frac{d}{dt}(\bar{R}^2)=[\frac{a^2-\bar{R}^2}{\ln\frac{a^2}{\bar{R}^2}}-\bar{R}^2]\frac{h'}{(1-\beta)h}-\frac{h^2}{(1-\beta)3\mu\ln\frac{a^2}{\bar{R}^2}}\times\left\{p_a-[p_v-\sigma(\frac{1}{\bar{R}}+\frac{2\cos\bar{\alpha}}{h})]\right\}\ \text{for}\ \bar{R}'>0 \tag{36}$$

$$\frac{d}{dt}(\bar{R}^2)=[\frac{a^2-\bar{R}^2}{\ln\frac{a^2}{\bar{R}^2}}-\bar{R}^2]\frac{h'}{h-\beta h_{past}}-\frac{h^3}{(h-\beta h_{past})3\mu\ln\frac{a^2}{\bar{R}^2}}\times\left\{p_a-[p_v-\sigma(\frac{1}{\bar{R}}+\frac{2\cos\bar{\alpha}}{h})]\right\}\ \text{for}\ \bar{R}'<0 \tag{37}$$

The derivation process of this equation is not described in detail here. This equation was also solved in this paper by MATLAB software and the result is shown in Fig. 11. It should be noted that the viscosity of ISO-VG #68 oil at ambient temperature (0.070 Pa·s)

was used in the calculation process in this paper while the viscosity of the lubricating oil at 40°C (0.049 Pa·s)was used in the Sun's work [Sun, Zhang, Chen et al. (2008)], which resulted in slightly different pressure variation calculated by Sun's model.

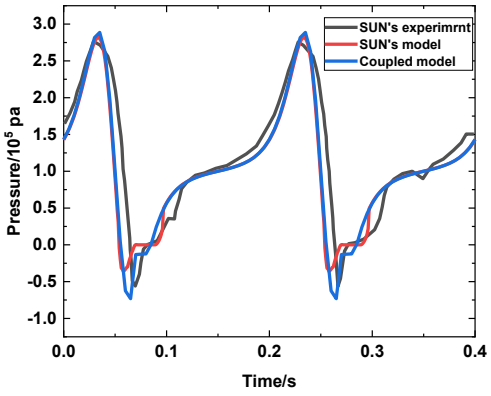

Figure 11: Pressure variation from Sun's experiment, Sun's model and coupled model

In Fig. 11, the black curve is the pressure curve obtained by Sun's experiment, while the red one is calculated by Sun's model, and the blue one is calculated by the model used in this paper. It should be pointed out that the pressure testing point of Sun's experiment is at a distance of 4.43 mm from the center of the lower plate, so the pressure results from the two models are also calculated based on this point. It is easy to find that there is a good coincidence among the three curves when the oil film pressure is positive, that is, when the upper plate moves downward. When the upper plate moves upward, the negative pressure appears, indicating that the oil film can withstand a certain tensile stress, and as the tensile stress continues to increase, the cavitation occurs. However, compared to Sun's model, the maximum negative pressure of the coupled model is larger, which is much closer to the experimentally measured data, and the calculated maximum negative pressure of Sun's model is smaller. In summary, the model in this paper can predict the pressure change more accurately than Sun's model and verify the reliability of the model for the oscillating squeeze oil film.

4 Discussion

The study of the oscillating squeezed oil film was mainly based on the theory of hydrodynamic lubrication in many papers. The influence of related parameters such as viscosity μ, oscillation squeeze frequency ω, amplitude ε and other factors on the pressure and cavitation in oil film has been extensively studied. However, in the process of modeling in this paper, the theory of bubble dynamics was introduced, and three new parameters, including surface dilatational viscosity, initial radii of cavitation nuclei and number of bubbles per unit area, were brought in this process. Therefore, it is necessary to study the effects of these new parameters on the pressure and cavitation area of the oscillating squeeze film. It is unfortunate that these three parameters introduced by the bubble dynamics, surface dilatational viscosity, initial radii of cavitation nuclei and number

of bubbles per unit area are difficult to measure by the existing methods, so the experimental research is difficult to carry out now. During calculation, The grid length along diameter direction was set to $\Delta x = L/1025$ as before, while the time step was set to $\Delta t = 1\times10^{-6}$ s. The change of oil film clearance at each time step was calculated by Eq. (34), while the equilibrium position h_0 is 250 μm, the amplitude ε is 125 μm and the frequency ω is 25 Hz. Except the parameters to be analyzed, the values of the other parameters' values are same in Tab. 3 and the specific calculation method is the same as above.

4.1 The effect of surface dilatational viscosity κ^s

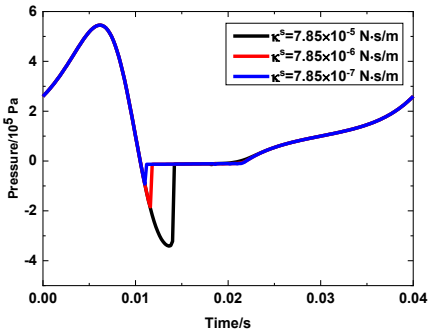

Figure 12: Pressure variation for different surface dilatational viscosity **(** h_0 =0.25 mm, ε =0.125 mm, ω=25 Hz**)**

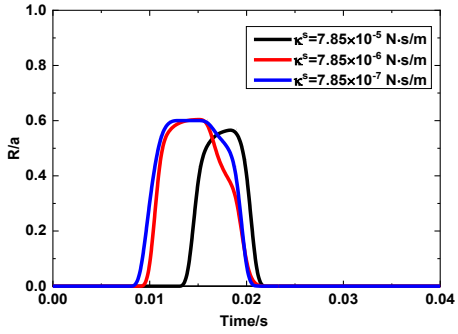

Figure 13: Cavitation area variation for different surface dilatational viscosity **(** h_0=0.25 mm, ε =0.125 mm, ω=25 Hz**)**

The effect of surface dilatational viscosity is shown in Fig. 12. The condition remains the same except for the clearance between two plates. Three different orders of magnitude of surface dilatational viscosity are taken. It can be seen that the change of surface dilatational viscosity does not affect the maximum positive value of the pressure in one cycle of the oscillatory oil squeeze film. However, it has a great influence on the maximum negative pressure. The results show that the larger the surface dilatational

viscosity is, the greater the negative pressure will be under the same conditions. It means that the increase in surface dilatational viscosity allows the lubricating oil to withstand greater tensile stress before the generation of cavitation, resulting in a delay in the generation of cavitation, as is shown in Fig. 13. Furthermore, large surface dilatational viscosity will reduce the duration of the cavitation. Nevertheless, the maximum cavitation area appears to be the same under different surface dilatational viscosities, which suggests that surface dilatational viscosity has no effect on the maximum cavitation area.

4.2 The effect of initial radii of cavitation nuclei R_0

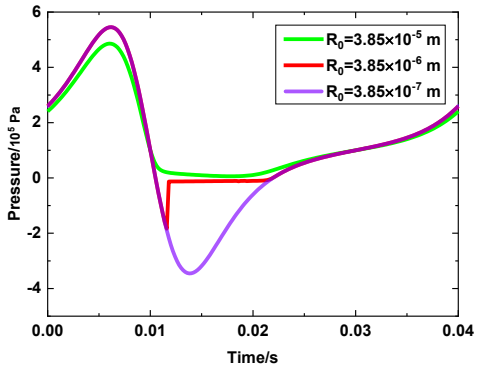

Figure 14: Pressure variation for different initial radii of cavitation nuclei **(** h_0 =0.25 mm, ε =0.125 mm, ω =25 Hz**)**

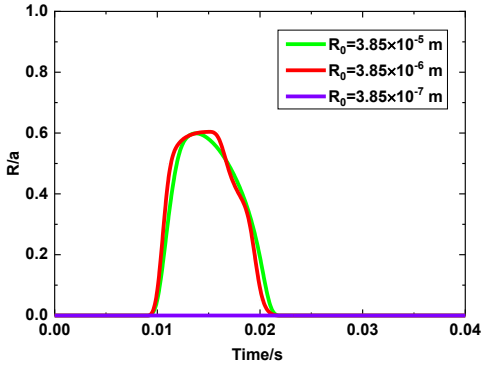

Figure 15: Cavitation area variation for different initial radii of cavitation nuclei **(** h_0 =0.25 mm, ε =0.125 mm, ω =25 Hz**)**

The effect of initial radii of cavitation nuclei is shown in Figs. 14 and 15. Three different orders of magnitude of surface dilatational viscosity are taken as before. It can be seen from Fig. 14 that the initial radii of cavitation nuclei have an influence both on the maximum and minimum pressures during one cycle. When the initial radii of cavitation

nuclei become larger, the maximum positive value of the pressure will drop slightly, which may result from decrease in the fraction variable. Meanwhile, the large bubble radius will significantly reduce the maximum negative pressure in one cycle. When the radius is large enough, there will be no negative pressure. On the contrary, when the radius is small, the oil film can withstand a large negative pressure without rupture, so there is no cavitation in this condition, as is shown in Fig. 15, which is in line with the experiments in squeeze film dampers [Diaz and San Andres (2001)].

4.3 The effect of number of bubbles per unit area n_b^s

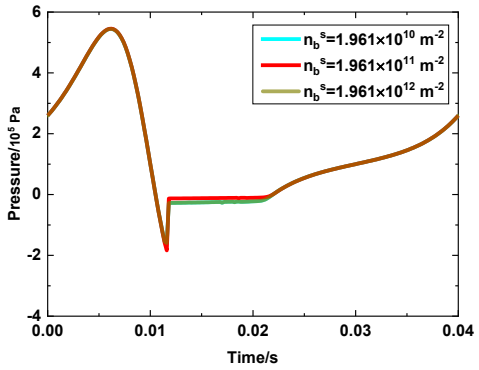

Figure 16: Pressure variation for different number of bubbles per unit area **(** h_0=0.25 mm, ε =0.125 mm, ω=25 Hz**)**

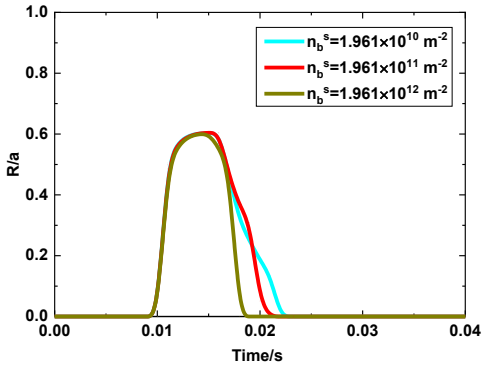

Figure 17: Cavitation area variation for different number of bubbles per unit area **(** h_0=0.25 mm, ε =0.125 mm, ω=25 Hz**)**

The effect of the number of bubbles per unit area is shown in Figs. 16 and 17. Three different orders of magnitude of number of bubbles per unit area are taken as before. It can be seen from Fig. 16 that three curves representing different number of bubbles per unit area almost coincide, which suggests that the change of the number of bubbles per

unit area has little effect on the pressure variation during one cycle. Moreover, the change of parameters will not change the appearance of the cavitation and the maximum cavitation area, as is shown in Fig. 17. However, it is notable that the number of bubbles per unit area affects the speed of the cavitation collapse. A large number of bubbles per unit area will accelerate the speed of cavitation collapse, which results in a decrease in the duration of the cavitation. Notice that a large number of bubbles per unit area may make the difference of cavitation collapse speed between model calculated and experiment become small in Fig. 9. However, it still cannot explain the stagnation of cavitation in the process of collapse in 0.4 seconds.

5 Conclusions

(1) A coupled cavitation model and a specific numerical calculation method were used to calculate pressure and cavitation in an oscillating squeeze oil film.

(2) A parallel-plate squeeze film test apparatus was used to verify the reliability and accuracy of the model. The result shows that the coupled cavitation model can well predict the generation, development and maximum area of cavitation. However, due to the neglect of the influence of the cavity inertial force and the local wall in the calculation process, the speed of cavitation collapse in experiments is slower than the model prediction, which needs to be improved in the future.

(3) The pressure curve predicted by the coupled model is compared with Sun's experiment and model. The results show that the pressure curve predicted by the coupled model is closer to the experimental value compared with Sun's cavitation model.

(4) Three new variables introduced by the theory of bubble dynamics are discussed, namely surface dilatational viscosity, initial radii of cavitation nuclei and number of bubbles per unit area. The calculation results show that surface dilatational viscosity, initial radii of cavitation nuclei and number of bubbles per unit area have a significant influence on the generation time of the cavitation, the maximum tensile stress that the oil film can withstand, and the speed of the cavitation collapse respectively.

Acknowledgement: Thanks for the support from Ford motor company, under Ford University Project 2014-2175R. The authors also gratefully acknowledge D. C. Sun, retired professor of State University of New York at Binghamton, for his encouragement and suggestions.

Funding Statement: Ford motor company, under Ford University Project 2014-2175R.

Conflicts of Interest: The authors declare that they have no conflicts of interest to report regarding the present study.

References

Bayada, G.; Chambat, M.; El Alaoui, M. (1990): Variational formulations and finite element algorithms for cavitation problems. *Journal of Tribology*, vol. 112, no. 2, pp. 398-403.

Braun, M.; Pierson, K.; Snyder, T. (2017): Two-way coupled reynolds, rayleigh-plesset-scriven and energy equations for fully transient cavitation and heat transfer modeling. *IOP*

Conference Series: Materials Science and Engineering, vol. 174, no. 1, 012030.

Braun, M. J.; Hannon, W. M. (2010): Cavitation formation and modeling for fluid film bearings: a review. *Proceedings of the Institution of Mechanical Engineers, Part J: Journal of Engineering Tribology*, vol. 224, no. 9, pp. 839-863.

Brewe, D. E. (1986): Theoretical modeling of the vapor cavitation in dynamically loaded journal bearings. *Journal of Tribology*, vol. 108, no. 4, pp. 628-638.

Chen, X. Y.; Sun, M. L.; Wang, W.; Sun, D. C.; Zhang, Z. M. et al. (2004): Experimental investigation of time-dependent cavitation in an oscillatory squeeze film. *Science in China Series G-Physics Mechanics & Astronomy*, vol. 47, no. 1, pp. 107-112.

Dellis, P. (2005): *Aspects of Lubrication in Piston Cylinder Assemblies (Ph.D. Thesis)*. Imperial College London, UK.

Dellis, P. (2019): Laser-induced fluorescence measurements in a single-ring test rig: evidence of cavitation and the effect of different operating conditions and lubricants in cavitation patterns and initiation. *International Journal of Engine Research*, vol. 20, no. 1, pp. 1-15.

Dellis, P.; Arcoumanis, C. (2005): Cavitation development in the lubricant film of a reciprocating piston-ring assembly. *Proceedings of the Institution of Mechanical Engineers, Part J: Journal of Engineering Tribology*, vol. 218, no. 3, pp. 157-171.

Diaz Briceno, S. E. (1999): *The Effect of Air Entrapment on the Performance of Squeeze Film Dampers: Experiments and Analysis (Ph.D. Thesis)*. Simon Bolívar University, Venezuela.

Diaz, S.; San Andres, L. (2001): A model for squeeze film dampers operating with air entrainment and validation with experiments. *Journal of Tribology*, vol. 123, no. 1, pp. 125-133.

Elrod, H. G. (1981): A cavitation algorithm. *Journal of Lubrication Technology*, vol. 103, no. 3, pp. 350-354.

Floberg, L. (1961): Boundary conditions of cavitation regions in journal bearings. *Asle Transactions*, vol. 4, no. 2, pp. 282-286.

Gehannin, J.; Arghir, M.; Bonneau, O. (2009): Evaluation of rayleigh-plesset equation based cavitation models for squeeze film dampers. *Journal of Tribology*, vol. 131, no. 2, pp. 02450-02451.

Gehannin, J.; Arghir, M.; Bonneau, O. (2016): A volume of fluid method for air ingestion in squeeze film dampers. *Tribology Transactions*, vol. 59, no. 2, pp. 208-218.

Geike, T.; Popov, V. (2009): Cavitation within the framework of reduced description of mixed lubrication. *Tribology International*, vol. 42, no. 1, pp. 93-98.

Geike, T.; Popov, V. L. (2009): A bubble dynamics based approach to the simulation of cavitation in lubricated contacts. *Journal of Tribology*, vol. 131, no. 1, 011704.

Hays, D. F.; Feiten, J. B. (1964): Cavities between moving parallel plates. *Cavitation in Real Liquids*, vol. 1, no. 1, pp. 122-137.

Jakobsson, B.; Floberg, L. (1957): The finite journal bearing, considering vaporization. *Transactions of Chalmers University of Technology*, vol. 117, no. 2, 190.

Jaramillo, A.; Buscaglia, G. C. (2019): A stable numerical strategy for reynolds-

rayleigh-plesset coupling. *Tribology International*, vol. 130, no. 1, pp. 191-205.

Kumar, A.; Booker, J. F. (1991): A finite element cavitation algorithm. *Journal of Tribology*, vol. 113, no. 2, pp. 276-284.

Natsumeda, S.; Someya, T. (1987): Negative pressures in statically and dynamically loaded journal bearings. *Tribology Series*, vol. 11, no. 1, pp. 65-72.

Olson, E. G.; Booker, J. F. (1997): Hydrodynamic analysis of journal bearings with structural inertia and elasticity by a modal finite element method. *Tribology Series*, vol. 32, pp. 661-673.

Olsson, K. O. (1965): Cavitation in dynamically loaded bearings. *Transactions of Chalmers University of Technology*, vol. 308, 60.

Parkins, D. W.; May Miller, R. (1984): Cavitation in an oscillatory oil squeeze film. *Journal of tribology*, vol. 106, no. 3, pp. 360-365.

Singhal, A. K.; Athavale, M. M.; Li, H. Y.; Jiang, Y. (2002): Mathematical basis and validation of the full cavitation model. *Journal of Fluids Engineering-Transactions of the Asme*, vol. 124, no. 3, pp. 617-624.

Snyder, T.; Braun, M. (2019): A CFD-based frequency response method applied in the determination of dynamic coefficients of hydrodynamic bearings. Part 1: theory. *Lubricants*, vol. 7, no. 3, pp. 23.

Snyder, T. A.; Braun, M. J.; Pierson, K. (2015): On rayleigh-plesset based cavitation modeling of fluid film bearings using the reynolds equation. *Journal of Physics: Conference Series*, vol. 656, no. 1, 012072.

Snyder, T. A.; Braun, M. J.; Pierson, K. C. (2016): Two-way coupled reynolds and rayleigh-plesset equations for a fully transient, multiphysics cavitation model with pseudo-cavitation. *Tribology International*, vol. 93, no. 1, pp. 429-445.

Sun, D.; Brewe, D. E.; Abel, P. B. (1994): Simultaneous pressure measurement and high-speed photography study of cavitation in a dynamically loaded journal bearing. *Journal of Tribology*, vol. 115, no. 1, pp. 88-95.

Sun, D. C.; Brewe, D. E. (1991): A high speed photography study of cavitation in a dynamically loaded journal bearing. *Journal of Tribology*, vol. 113, no. 2, pp. 287-292.

Sun, D. C.; Brewe, D. E. (1992): Two reference time scales for studying the dynamic cavitation of liquid films. *Journal of Tribology*, vol. 114, no. 3, pp. 612-615.

Sun, D. C.; Wang, W.; Zhang, Z. M.; Chen, X. Y.; Sun, M. L. (2008): Theory of cavitation in an oscillatory oil squeeze film. *Tribology Transactions*, vol. 51, no. 3, pp. 332-340.

Sun, M.; Zhang, Z.; Chen, X.; Wang, W.; Meng, K. et al. (2008): Experimental study of cavitation in an oscillatory oil squeeze film. *Tribology Transactions*, vol. 51, no. 3, pp. 341-350.

Vijayaraghavan, D.; Keith Jr, T. G. (1989): Development and evaluation of a cavitation algorithm. *Tribology Transactions*, vol. 32, no. 2, pp. 225-233.

Vincent, B.; Maspeyrot, P.; Frene, J. (1996): Cavitation in dynamically loaded journal bearings using mobility method. *Wear*, vol. 193, no. 2, pp. 155-162.

Wang, W.; Zhang, Z.; Chen, X.; Sun, M.; Sun, D. C. (2005): Investigation of

cavitation phenomenon in an oscillatory oil squeeze film. *World Tribology Congress III*, pp. 575-576.

Zarbane, K.; Zeghloul, T.; Hajjam, M. (2011): A numerical study of lubricant film behaviour subject to periodic loading. *Tribology International*, vol. 44, no. 12, pp. 1659-1667.

Zarbane, K.; Zeghloul, T.; Hajjam, M. (2013): Experimental study of lubricant film behaviour subject to periodic loading. *Proceedings of the Institution of Mechanical Engineers, Part J: Journal of Engineering Tribology*, vol. 227, no. 6, pp. 538-547.

Zwart, P. J.; Gerber, A. G.; Belamri, T. (2004): A two-phase flow model for predicting cavitation dynamics. *Fifth International Conference on Multiphase Flow*, vol. 152.